Metal Organic Frameworks Route to *in Situ* Insertion of Multiwalled Carbon Nanotubes in Co_3O_4 Polyhedra as Anode Materials for Lithium-Ion Batteries

Gang Huang,[†,‡] Feifei Zhang,[†,‡] Xinchuan Du,[†,‡] Yuling Qin,[†] Dongming Yin,[†] and Limin Wang[*,†,§]

[†]State Key Laboratory of Rare Earth Resource Utilization, Changchun Institute of Applied Chemistry, Chinese Academy of Sciences, Changchun, 130022, People's Republic of China, [‡]University of Chinese Academy of Sciences, Beijing, 100049, People's Republic of China, and [§]Changzhou Institute of Energy Storage Materials and Devices, Changzhou, 213000, People's Republic of China

ABSTRACT Hybridizing nanostructured metal oxides with multiwalled carbon nanotubes (MWCNTs) is highly desirable for the improvement of electrochemical performance of lithium-ion batteries. Here, a facile and scalable strategy to fabricate hierarchical porous MWCNTs/Co_3O_4 nanocomposites has been reported, with the help of a morphology-maintained annealing treatment of carbon nanotubes inserted metal organic frameworks (MOFs). The designed MWCNTs/Co_3O_4 integrates the high theoretical capacity of Co_3O_4 and excellent conductivity as well as strong mechanical/chemical stability of MWCNTs. When tested as anode materials for lithium-ion batteries, the nanocomposite displays a high reversible capacity of 813 mAh g^{-1} at a current density of 100 mA g^{-1} after 100 charge–discharge cycles. Even at 1000 mA g^{-1}, a stable capacity as high as 514 mAh g^{-1} could be maintained. The improved reversible capacity, excellent cycling stability, and good rate capability of MWCNTs/Co_3O_4 can be attributed to the hierarchical porous structure and the synergistic effect between Co_3O_4 and MWCNTs. Furthermore, owing to this versatile strategy, binary metal oxides MWCNTs/$ZnCo_2O_4$ could also be synthesized as promising anode materials for advanced lithium-ion batteries.

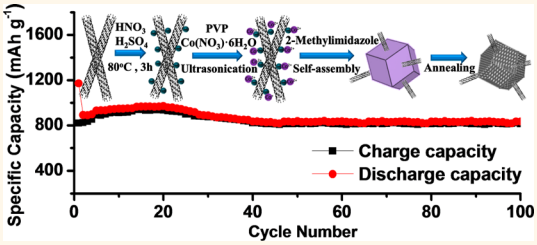

KEYWORDS: metal–organic frameworks · MWCNTs/Co_3O_4 · MWCNTs/$ZnCo_2O_4$ · anode materials · Li-ion batteries

Since the emergence of lithium-ion batteries (LIBs), efforts to design and explore new electrode materials with high electrochemical performance have not stopped.[1−4] Recently, the burgeoning market for small mobile devices and the development of electric vehicles require further enhancement in terms of energy and power density of the LIBs. However, due to the relatively low theoretical capacity of graphite, the current commercial LIBs have reached their performance limit. As a result, there is an immediate need to develop anode materials capable of delivering higher energy density and longer cycling life. To this end, transition metal oxides especially Co_3O_4 have been focused on as promising anode materials for LIBs because of their high electrochemical capacities.[5−8] Unfortunately, the poor electrical conductivity and the huge volume change associated with Li^+ insertion/extraction of the transition metal oxides stand in the way of their commercialization. There are different approaches to circumvent these issues: one solution is to fabricate hierarchical porous structures composed of nanosized building blocks, such as pompon-like Co_3O_4 porous spheres,[9] nanosheet-assembled multishelled Co_3O_4 hollow spheres,[10] and mesoporous Co_3O_4 architectures.[11] Other solutions are coating/supporting transition metal oxides with various carbon materials, because the introduced carbonaceous materials can not only provide continuous electron transport channels but also buffer the volume change during charge–discharge cycles.[12−14] Although the above approaches have been proven more or less effective, there is still plenty room for further improvement.

Metal organic frameworks (MOFs), a class of crystalline inorganic–organic hybrid materials, characterized by diverse skeletal and well-defined pore structures with high surface areas and large pore volume, are very attractive for applications in catalysis,[15,16]

* Address correspondence to lmwang@ciac.ac.cn.

Received for review November 2, 2014 and accepted January 28, 2015.

Published online January 28, 2015
10.1021/nn506252u

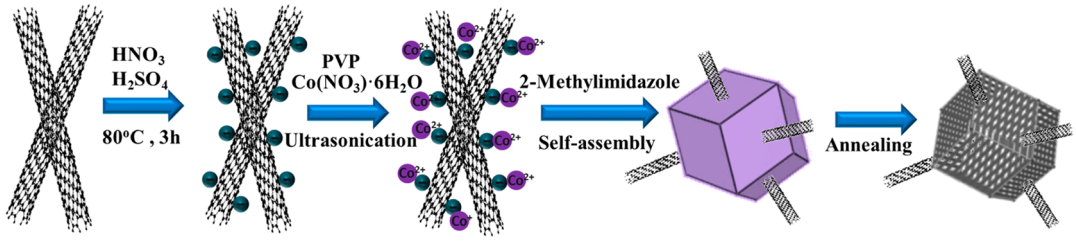

Figure 1. Schematic illustration of the procedure used to fabricate MWCNTs/Co_3O_4.

gas adsorption and separation,[17,18] drug delivery,[19] and energy storage.[20−22] Moreover, MOFs feature exceptional specific surface areas and pore volume, and using them as precursors/templates provides a unique opportunity to develop a novel kind of highly tailorable metal oxides.[23−28] For example, Fe_2O_3@Ni-Co_2O_4 nanoboxes,[25] $NiFe_2O_4$@Fe_2O_3 nanotubes,[26] and symmetric porous ternary $Zn_xCo_{3-x}O_4$ hollow polyhedra[29] have been fabricated by choosing suitable MOFs as templates, exhibiting enhanced electrochemical performance as anode materials for LIBs. Despite the progress achieved to date, the generation of metal oxides/multiwalled carbon nanotubes (MWCNTs) composite from MWCNTs/MOFs has rarely succeeded due to the chemically inert and highly hydrophobic nature of pristine MWCNTs, making it difficult to deposit materials on their surface directly.

Herein, MWCNTs/ZIF-67 has been successfully fabricated based on a facile and scalable coprecipitation of Co ions and 2-methylimidazolate in the presence of MWCNTs, and then MWCNTs/Co_3O_4 is obtained by thermal treatment of the as-synthesized MWCNTs/ZIF-67. The Co_3O_4 polyhedra with MWCNTs inserted turn out to be hierarchical porous structures consisting of small nanoparticle building blocks. When applied as anode materials for LIBs, MWCNTs/Co_3O_4 manifests high capacity and excellent cycling stability and rate capability. With the successful synthesis of MWCNTs/Co_3O_4 as a starting point, this facile strategy can be used to generate binary metal oxides MWCNTs/$ZnCo_2O_4$ with superior lithium storage properties.

RESULTS AND DISCUSSION

The strategy for synthesizing MWCNTs/Co_3O_4 is schematically depicted in Figure 1. First, electronegative carboxylic groups (−COOH) are functionalized on the MWCNTs' surface *via* acid treatment to serve as nucleation centers for loading MOFs.[30] Then, the treated MWCNTs are homogeneously dispersed in methanol in the presence of $Co(NO_3)_2·6H_2O$ and PVP through ultrasonic treatment, and Co^{2+} adsorbs onto the functional groups of MWCNTs due to an electrostatic interaction. Subsequently, 2-methylimidazolate methanol solution is added to allow for heterogeneous nucleation, and the small ZIF-67 located on the surface of MWCNTs serves as crystal nuclei for the growth of ZIF-67 polyhedra in the stewing process. As a result, the long MWCNTs are *in situ* self-inserted into the ZIF-67 crystal. Ultimately, MWCNTs/Co_3O_4 is obtained from MWCNTs/ZIF-67 by conducting a calcinating process at 400 °C in air.

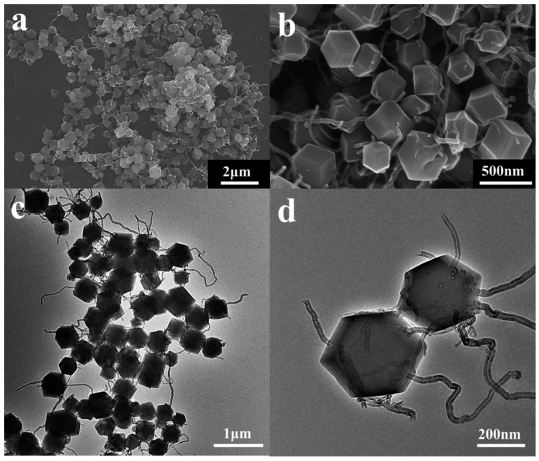

Figure 2. (a, b) SEM and (c, d) TEM images of the as-synthesized MWCNTs/ZIF-67.

The phase identification of the MWCNTs/ZIF-67 is examined by powder X-ray diffraction (XRD). As shown in Figure S1 (Supporting Information), all diffraction peaks with strong intensities match well with the simulated ZIF-67,[23] indicating the pure phase and high crystallinity of ZIF-67. Furthermore, the broad peak located at around 26.5° corresponds to the typical (002) facet of the MWCNTs. The representative SEM images of MWCNTs/ZIF-67 are shown in Figure 2a and b. They indicate that the MWCNTs/ZIF-67 nanocomposite consists of uniform MWCNT-inserted polyhedra with a perfectly smooth surface and a size of approximately 500 nm. To give further insight into the morphology and structure of the as-synthesized MWCNTs/ZIF-67, TEM analysis has been carried out. Figure 2c reveals that the homogeneously distributed ZIF-67 are solid polyhedra intertwined with MWCNTs. The magnified TEM image in Figure 2d confirms that the intertwined MWCNTs are inserted in ZIF-67 polyhedra, forming a novel MWCNTs/ZIF-67 nanocomposite.

The thermogravimetric (TG) curves in Figure S2 (Supporting Information) reveal the thermal behavior of MWCNTs/ZIF-67 and MWCNTs. The MWCNTs/ZIF-67 could remain stable at about 350 °C. Subsequently, there is a steep weight loss when the temperature rises

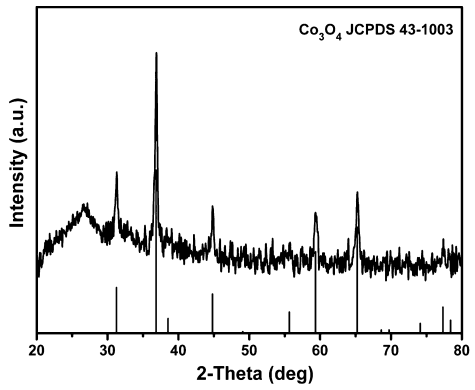

Figure 3. XRD pattern of the as-synthesized MWCNTs/Co_3O_4.

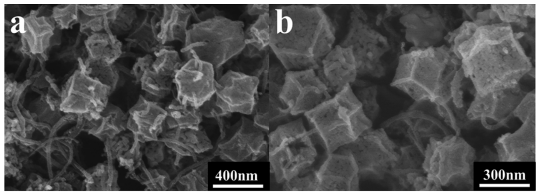

Figure 4. SEM images of the as-synthesized MWCNTs/Co_3O_4.

to 400 °C, ascribed to the oxidation of the organic linker into CO_2 and H_2O. On further increasing the temperature, the MWCNTs begin to degrade at around 450 °C. For pure MWCNTs, almost no weight loss associated with the decomposition of MWCNTs is observed when the temperature is below 500 °C. These results suggest that the MWCNTs can be well maintained at 400 °C, while the ZIF-67 can be completely decomposed to oxides. On the basis of TG analysis, 400 °C is chosen as the calcinating temperature to obtain the final products. To analyze the crystal structure of the annealed products, XRD measurement has been performed (Figure 3). The characteristic broad peak around 26.5 °C certifies the existence of MWCNTs in the annealed products. All the other peaks can be perfectly indentified as spinel Co_3O_4 (JCPDS No.43-1003), and there are no additional peaks from impurities, suggesting the high purity of Co_3O_4 and the formation of the MWCNTs/Co_3O_4 nanocomposite.

Figure 4 shows the SEM images of the MWCNTs/Co_3O_4. It can be seen that the annealed products well maintain size homogeneity and structural morphology of MWCNTs/ZIF-67 even after a high-temperature calcinating process. The increased surface roughness and the tiny holes on the surface of MWCNTs/Co_3O_4 can be ascribed to the liberation of CO_2 and H_2O during thermal treatment. In addition, the magnified SEM image in Figure 4b indicates that the MWCNTs are intertwined with the Co_3O_4 polyhedra. As revealed by TEM images in Figure 5a and b, the MWCNTs/Co_3O_4 with MWCNTs inserted and intertwined has a hierarchical porous structure, and each Co_3O_4 polyhedron is composed of small building blocks with sizes of 5−10 nm. Figure 5c and d give the HRTEM images

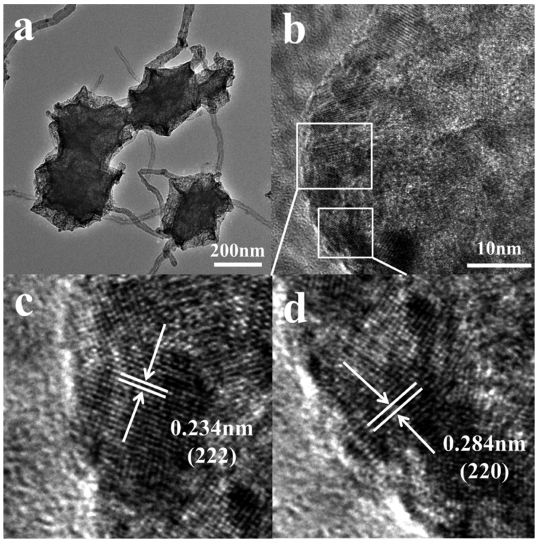

Figure 5. (a, b) TEM and (c, d) HRTEM images of the as-synthesized MWCNTs/Co_3O_4.

recorded from the white-framed area marked in Figure 5b. The measured *d*-spacings of two randomly selected nanoparticles are 0.234 and 0.284 nm, corresponding well to the (222) and (220) planes of Co_3O_4, respectively. All in all, the novel MWCNTs/Co_3O_4 composite can be obtained by a simple calcination of the MWCNTs/ZIF-67 precursor. The content of MWCNTs in the MWCNTs/Co_3O_4 nanocomposite is estimated to be ~5.6% by TG analysis as presented in Figure S2 (Supporting Information).

N_2 adsorption−desorption measurement has been taken to characterize the specific surface areas and pore size distribution of MWCNTs/Co_3O_4. As shown in Figure S3a, a type IV isotherm with a distinct hysteresis loop in the relative pressure region of $0.75 < P/P_0 < 0.98$ occurs for MWCNTs/Co_3O_4, indicating the mesoporous characteristics. The Brunauer−Emmett−Teller (BET) surface areas and total pore volume of MWCNTs/Co_3O_4 are 62.9 $m^2\ g^{-1}$ and 0.31 $cm^3\ g^{-1}$, respectively. The pore size distribution calculated from the Barrett−Joyner−Halenda (BJH) method shows that the MWCNTs/Co_3O_4 are hierarchical porous composites with a narrow distribution centered at 3.5 nm, a wide distribution centered around 15 nm, and also some macropores (Figure S3b, Supporting Information). The small pores may come from the liberation of gases during the oxidation decomposition of organic linkers in the calcinating process, while the large pores may be attributed to the inner diameter of the MWCNTs and the connection of adjacent small pores. The moderate surface areas endow MWCNTs/Co_3O_4 with a large electrode/electrolyte contact area, while the hierarchical porous characteristics can facilitate the transport of Li^+ and the penetration of electrolyte molecules as well as buffer the volume change during the repeated Li^+ insertion/extraction.

Motivated by the structural and compositional advantages of MWCNTs/Co_3O_4, cyclic voltammetric (CV)

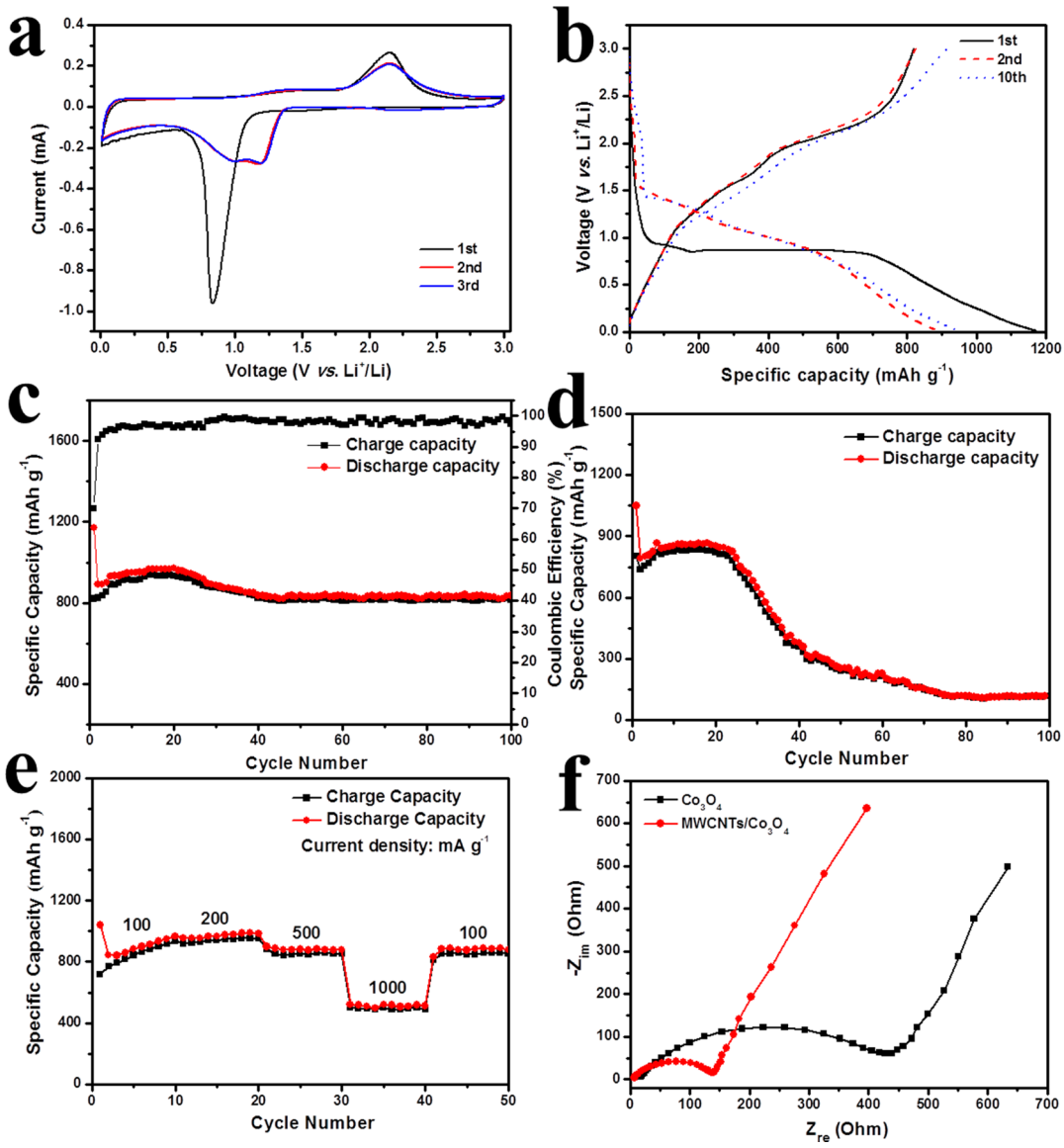

Figure 6. (a) Representative cyclic voltammograms (CVs) of the MWCNTs/Co_3O_4 at a scan rate of 0.1 mV s^{-1} between 0.01 and 3 V *vs* Li/Li^+. (b) Charge−discharge voltage profiles of the MWCNTs/Co_3O_4 for the first, second, and 10th cycles in the voltage range 0.01−3 V at a current rate of 100 mA g^{-1}. (c) Capacity and Coulombic efficiency *vs* cycle number of the MWCNTs/Co_3O_4 at a current rate of 100 mA g^{-1}. (d) Capacity *vs* cycle number of the Co_3O_4 at a current rate of 100 mA g^{-1}. (e) Rate capability of the MWCNTs/Co_3O_4. (f) Electrochemical impedance spectra (Nyquist plots) of Co_3O_4 and MWCNTs/Co_3O_4 at full charge state.

and galvanostatic charge−discharge measurements have been performed to evaluate their lithium storage performance as anode materials. The first three consecutive CV curves of MWCNTs/Co_3O_4 nanocomposites are given in Figure 6a. In the first cathodic sweep, there is only one intense peak around 0.84 V, corresponding to the reduction of Co_3O_4 to metallic Co dispersed in an amorphous Li_2O matrix and the formation of a solid electrolyte interface (SEI) film.[14,31] This cathodic peak is replaced by two broad peaks split near 1.1 V with significantly decreased intensity in the subsequent cycles, indicating the multistep reaction behavior during the discharge process and the occurrence of some irreversible transformation and structure modification in the first cycle.[14,32] During the anodic process, the peak at 2.15 V represents the oxidation of Co to Co_3O_4 and the decomposition of the Li_2O matrix.[31] Apart from the first cycle, all peaks are stable and reproducible in the following cycles, implying that the MWCNTs/Co_3O_4 nanocomposite exhibits good electrochemical reversibility. On the basis of the above analysis and CV curves, together with the previously reported storage mechanism of Co_3O_4,[11,14,31,32] the electrochemical reactions involved in the charge−discharge process can be expressed as follows:

$$Co_3O_4 + 8Li^+ + 8e^- \leftrightarrow 4Li_2O + 3Co \qquad (1)$$

Figure 6b displays selected representative charge−discharge profiles of MWCNTs/Co_3O_4 measured between 0.01 and 3 V at a current density of 100 mA g^{-1}.

There is a long flat voltage plateau at 0.85 V in the first discharge curve, followed by a gradually decrease until the end of the discharge. The discharge voltage plateau becomes steeper and shifts close to 1.25 V in the subsequent cycles, probably due to the structural and compositional variation of the electrode materials in the initial cycle,[33] which is consistent with the CV curves. The first discharge and charge capacities are 1171 mAh g^{-1} and 812 mAh g^{-1} based on the total mass of the composite electrode, corresponding to an irreversible capacity loss of 30%, which is probably ascribed to the formation of SEI films, some undecomposed Li_2O phase, and the irreversible decomposition of the electrolyte.[34]

Figure 6c depicts the charge−discharge capacities *versus* cycle number profiles of MWCNTs/Co_3O_4 at a current density of 100 mA g^{-1}. The composite electrode exhibits a capacity rise in the first 20 cycles. Such a capacity rise could be due to the improvement of Li^+ accessibility and accommodation behavior in the composite electrode, the transformation of the crystalline structure to an amorphous structure of MWCNTs/Co_3O_4, and the formation of a gel-like surface film during the initial activation process.[12,35] Then the capacity slowly decreases and stabilizes at 821 mAh g^{-1} in the 40th cycle, which is attributed to the stable formation of a gel-like film and the fulfillment of phase and structure transformations of the electrode material. After that, the discharge capacity stabilizes at around 820 mAh g^{-1} in the following 60 cycles, and a high capacity of 813 mAh g^{-1} is still achieved in the 100th cycle. Furthermore, from the fifth cycle onward, the Coulombic efficiency of the MWCNTs/Co_3O_4 is above 95%, indicating the excellent reversible Li^+ insertion/extraction of the composite electrode. Note that due to the low content of MWCNTs in the MWCNTs/Co_3O_4 nanocomposite and the small specific capacity of MWCNTs in the same voltage range (~130 mAh g^{-1}, Figure S5, Supporting Information), the contribution the MWCNTs make to the capacity of MWCNTs/Co_3O_4 is negligible, while for Co_3O_4 derived from ZIF-67 (Figure S4, Supporting Information), the specific capacity exhibits a continuous decline and decreases from the initial 1049 mAh g^{-1} to 118 mAh g^{-1} after 100 cycles (Figure 6d). These results indicate that the cycling life can be remarkably improved by inserting MWCNTs in Co_3O_4.

The rate capability of the MWCNTs/Co_3O_4 at progressively increased current densities is shown in Figure 6e. The MWCNTs/Co_3O_4 exhibits decent capacity retention with average discharge capacities of 913, 971, and 882 mAh g^{-1} at 100, 200, and 500 mA g^{-1}, separately. Even at a high current density of 1000 mA g^{-1}, a discharge capacity of 514 mAh g^{-1} could still be delivered. After that, the discharge capacity resumes well to 879 mAh g^{-1} when the current density is lowered to 100 mA g^{-1}. The excellent cycling and rare performances render MWCNTs/Co_3O_4 as promising anode materials for future LIBs.

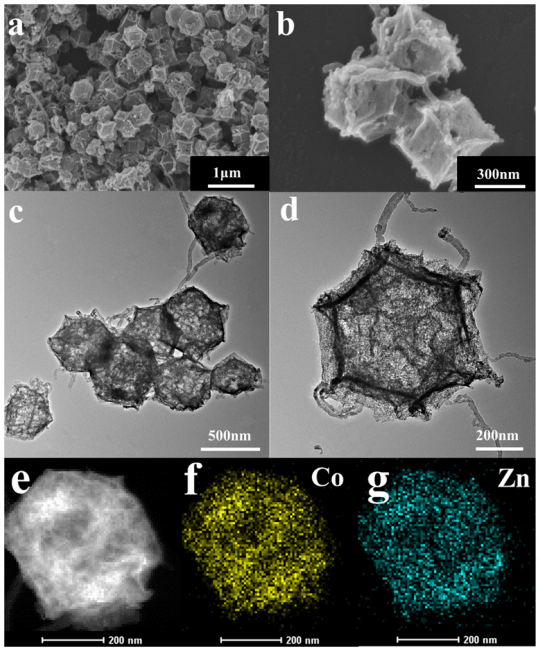

Figure 7. (a, b) SEM; (c, d) TEM; and (e) HAADF-STEM images of the as-synthesized MWCNTs/$ZnCo_2O_4$; (f, g) element mappings of the as-synthesized MWCNTs/$ZnCo_2O_4$.

To probe the kinetic properties of MWCNTs/Co_3O_4 and Co_3O_4, electrochemical impedance spectroscopy (EIS) measurements have been conducted. Both plots in Figure 6f are composed of a semicircle at the high to medium frequencies followed by a sloped line at low frequencies. The semicircle is associated with the charge transfer resistance at the interface between electrode and electrolyte, and the sloped line is ascribed to the diffusion resistance related to the Li^+ diffusion in the electrode. It can be clearly seen that both MWCNTs/Co_3O_4 and Co_3O_4 exhibit similar diffusion resistance, but the charge transfer resistance of MWCNTs/Co_3O_4 is much smaller, which indicates that the inserted MWCNTs could boost the electronic conductivity and enable much easier charge transfer at the electrode/electrolyte interface. Thus, the improved electronic conductivity is considered to be a key factor in improving the electrochemical performance of Co_3O_4.

Our protocol can be further extended to the fabrication of MWCNTs/$ZnCo_2O_4$ (Figures S9 and S10, Supporting Information) using heterobimetallic MWCNTs/ZIF-67 (Zn, Co) as precursor (Figures S6−8, Supporting Information). SEM images in Figure 7a and b reveal that MWCNTs/$ZnCo_2O_4$ with a uniform distribution has the same morphology as MWCNTs/Co_3O_4. The surface of the $ZnCo_2O_4$ polyhedra is rough and intertwined with MWCNTs. The TEM images (Figure 7c and d) further characterize the detailed morphology and structure of MWCNTs/$ZnCo_2O_4$. They indicate that $ZnCo_2O_4$ polyhedra with hierarchical porous structure contain

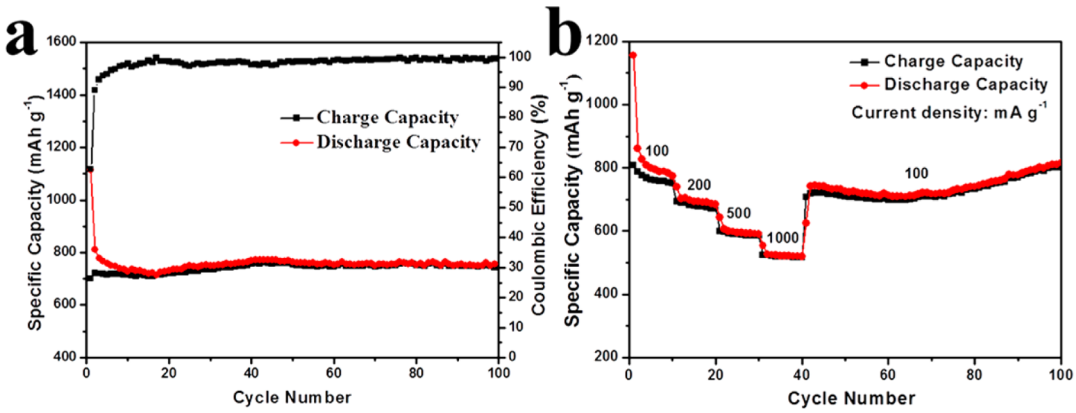

Figure 8. (a) Capacity and Coulombic efficiency *vs* cycle number of the MWCNTs/$ZnCo_2O_4$ at a current rate of 100 mA g^{-1}. (b) Rate capability of the MWCNTs/$ZnCo_2O_4$.

MWCNTs, confirming the successful synthesis of MWCNTs/$ZnCo_2O_4$ composites. Moreover, the element mappings in Figure 7f and g demonstrate the homogeneous dispersion and coexistence of Zn and Co through the whole selected MWCNTs/$ZnCo_2O_4$ particle. The energy-dispersive X-ray spectroscopy (EDS) spectrum has been used to determine the Zn/Co atomic ratio in the MWCNTs/$ZnCo_2O_4$ composite. It shows strong signals of C, O, Co, and Zn elements (Figure S10c, Supporting Information). Calculated from the EDS result, the ratio of Zn/Co is about 1:1.91, in close agreement with the expected stoichiometric ratio of the $ZnCo_2O_4$ phase.

The electrochemical properties of MWCNTs/$ZnCo_2O_4$ are examined by galvanostatic charge–discharge measurement. Figure 8a shows the cycling performance of MWCNTs/$ZnCo_2O_4$ at 100 mA g^{-1}. It is found that during the whole charge–discharge process, the discharge capacity of MWCNTs/$ZnCo_2O_4$ is stable near 760 mAh g^{-1}, and a capacity of 755 mAh g^{-1} could be achieved even after 100 cycles, indicating the excellent capacity retention of MWCNTs/$ZnCo_2O_4$. The rate capability of MWCNTs/$ZnCo_2O_4$ is depicted in Figure 8b. As can be seen, the average discharge capacity of MWCNTs/$ZnCo_2O_4$ decreases from 839 to 526 mAh g^{-1} as the current density gradually increases from 100 to 1000 mA g^{-1}. After enduring various charge–discharge rates, the composite electrode recovers its capacity to 745 mAh g^{-1} with the rate back to 100 mA g^{-1} and maintains this value with little increase up to 100 cycles.

The superior electrochemical performance of MWCNTs/MCo_2O_4 (M = Zn, Co) is believed to originate from its hierarchical porous structure and the synergistic interaction of MCo_2O_4 and MWCNTs: (i) the nanosized building blocks could improve the kinetics of charge transfer and shorten the Li^+ diffusion distance; (ii) the addition of MWCNTs may protect MCo_2O_4 from aggregation and disintegration as well as partially buffer the stress induced by the volume change during cycles; (iii) the MWCNTs in MCo_2O_4 improve the conductivity of the composite and thus enhance the electron transfer rate; (iv) the hierarchical porous structure enhances the electrode/electrolyte contact area, provides abundant channels for electrolyte penetration, and also relaxes the stress and alleviates the structure decomposition induced by Li^+ insertion/extraction. All the above factors contribute to the enhanced lithium storage performance of MWCNTs/MCo_2O_4.

CONCLUSIONS

In summary, hierarchical porous MWCNTs/MCo_2O_4 (M = Zn, Co) nanocomposite has been successfully synthesized by thermal treatment of the MWCNTs/ZIF-67 precursor. In this nanocomposite, the MWCNTs are inserted in the MCo_2O_4 polyhedra, forming a hierarchical porous structure with nanosized building blocks. Electrochemical measurements demonstrate that MWCNTs/MCo_2O_4 exhibits superior lithium storage performance in terms of specific capacity, cycling stability, and rate capability. The excellent electrochemical performance is attributed to the rational combination of the advantages of the hierarchical porous structure and the synergistic interaction between MCo_2O_4 and MWCNTs. Our work presents a facile and affordable general technique for the preparation of other MWCNTs/metal oxide composites that hold great promise in the field of energy storage and electrical devices.

EXPERIMENTAL METHODS

Pretreatment of MWCNTs. A 0.3 g amount of pristine multiwalled carbon nanotubes was soaked in a 50 mL mixture of nitric acid and sulfuric acid (3:1) in a water bath at 80 °C for 3 h with stirring. The resulting products were collected by filtration and washed with deionized water several times, then dried at 80 °C overnight.

Synthesis of MWCNTs/ZIF-67. In a typical procedure, 35 mg of pretreated MWCNTs and 175 mg of PVP were dissolved in 25 mL of methanol solution. After the MWCNTs were uniformly dispersed with the assistance of ultrasonication for 0.5 h, the resultant solution was mixed with 498 mg of $Co(NO_3)_2 \cdot 6H_2O$. Then the solution was stirred for 1 h at room temperature to form a black solution, A. Subsequently, 765 mg of 2-methylimidazole was dissolved in 25.0 mL of methanol to form a clear solution, B, followed by the slow addition to solution A under stirring for 30 min. Being kept still for 24 h, the obtained precipitate was collected by centrifugation, washed thoroughly with methanol several times to remove the surfactant and the residual ions, and finally dried at 70 °C for 12 h. For comparison, a ZIF-67 polyhedron was synthesized by a similar protocol without the addition of MWCNTs.

Synthesis of MWCNTs/Co_3O_4. A porcelain boat loaded with the powder of MWCNTs/ZIF-67 was placed in a muffle furnace and then heated to 400 °C with a ramp of 2 °C min^{-1} and maintained for 1 h. After that, the furnace was allowed to cool to room temperature naturally. Last, the product was taken out and the MWCNTs/Co_3O_4 was obtained. The same procedure was conducted to convert ZIF-67 to Co_3O_4.

Materials Characterization. XRD patterns were collected on a Bruker D8 Focus powder X-ray diffractometer using Cu Kα radiation. The morphology and microstructure of the samples were investigated by a Hitachi S-4800 field emission scanning electron microscope at an accelerating voltage of 10 kV. Transmission electron microscopy (TEM), high-angle annular dark-field scanning transmission electron microscopy (HAADF-STEM), energy-dispersive X-ray spectroscopy (EDS) element mapping and spectra were performed on a FEI Tecnai G2 S-Twin instrument with a field emission gun operating at 200 kV. Thermogravimetric analysis was performed in air from 25 to 800 °C with a heating rate of 10 °C min^{-1} by using an STA 449 Jupiter (NETZSCH) thermogravimetry analyzer. N_2 adsorption–desorption isotherms were obtained with a Micromeritics ASAP 2010 instrument at −196 °C. Prior to the measurement, the sample was pretreated at 150 °C for 2 h under vacuum.

Electrochemical Measurements. The electrochemical behaviors of the MWCNTs/MCo_2O_4 (M = Zn, Co) were examined by using CR 2025 coin-type cells with pure lithium foil as the counter electrode, a Celgard 2400 membrane as the separator, and 1 M $LiPF_6$ dissolved in ethyl carbonate and diethyl carbonate (1:1 in volume) as the electrolyte. The working electrode was prepared by compressing a mixture of the active materials, carbon black, and poly(vinylidene fluoride) with a weight ratio of 70:20:10 onto a copper foil and drying in a vacuum oven at 80 °C for 12 h. Then the cells were assembled in a glovebox filled with highly pure argon gas. The cyclic voltammogram and electrochemical impedance spectral measurements were conducted on a BioLogic VMP3 electrochemical workstation. The charge–discharge performance was tested between 0.01 and 3 V using the LAND CT2001A multichannel battery testing system at room temperature.

Conflict of Interest: The authors declare no competing financial interest.

Acknowledgment. This work is supported by the National Nature Science Foundation of China (Grant No. 20111061).

Supporting Information Available: Supporting Information including XRD patterns, SEM images, TEM images, TGA curve, N_2 adsorption–desorption isotherms, pore size distribution curve, and EDS analysis is provided. This material is available free of charge *via* the Internet at http://pubs.acs.org.

REFERENCES AND NOTES

1. Bruce, P. G.; Scrosati, B.; Tarascon, J. M. Nanomaterials for Rechargeable Lithium Batteries. *Angew. Chem., Int. Ed.* **2008**, *47*, 2930–2946.
2. Ji, L. W.; Lin, Z.; Alcoutlabi, M.; Zhang, X. W. Recent Developments in Nanostructured Anode Materials for Rechargeable Lithium-Ion Batteries. *Energy Environ. Sci.* **2011**, *4*, 2682–2699.
3. Lu, Y.; Tu, J. P.; Xiong, Q. Q.; Xiang, J. Y.; Mai, Y. J.; Zhang, J.; Qiao, Y. Q.; Wang, X. L.; Gu, C. D.; Mao, S. X. Controllable Synthesis of a Monophase Nickel Phosphide/Carbon (Ni_5P_4/C) Composite Electrode *via* Wet-Chemistry and a Solid-State Reaction for the Anode in Lithium Secondary Batteries. *Adv. Funct. Mater.* **2012**, *22*, 3927–3935.
4. Xiong, Q. Q.; Tu, J. P.; Xia, X. H.; Zhao, X. Y.; Gu, C. D.; Wang, X. L. A Three-Dimensional Hierarchical Fe_2O_3@NiO Core/Shell Nanorod Array on Carbon Cloth: A New Class of Anode for High-Performance Lithium-Ion Batteries. *Nanoscale* **2013**, *5*, 7906–7912.
5. Wu, H. B.; Chen, J. S.; Hng, H. H.; Lou, X. W. Nanostructured Metal Oxide-Based Materials as Advanced Anodes for Lithium-Ion Batteries. *Nanoscale* **2012**, *4*, 2526–2542.
6. Cabana, J.; Monconduit, L.; Larcher, D.; Palacín, M. R. Beyond Intercalation-Based Li-Ion Batteries: The State of the Art and Challenges of Electrode Materials Reacting through Conversion Reactions. *Adv. Mater.* **2010**, *22*, E170–E192.
7. Wang, Z. Y.; Zhou, L.; Lou, X. W. Metal Oxide Hollow Nanostructures for Lithium-Ion Batteries. *Adv. Mater.* **2012**, *24*, 1903–1911.
8. Yin, L. W.; Zhang, Z. W.; Li, Z. Q.; Hao, F. B.; Li, Q.; Wang, C. X.; Fan, R. H.; Qi, Y. X. Spinel $ZnMn_2O_4$ Nanocrystal-Anchored 3D Hierarchical Carbon Aerogel Hybrids as Anode Materials for Lithium Ion Batteries. *Adv. Funct. Mater.* **2014**, *26*, 4176–4185.
9. Hao, W. J.; Chen, S. M.; Cai, Y. J.; Zhang, L.; Li, Z. X.; Zhang, S. J. Three-Dimensional Hierarchical Pompon-Like Co_3O_4 Porous Spheres for High-Performance Lithium-Ion Batteries. *J. Mater. Chem. A* **2014**, *2*, 13801–13804.
10. Wang, X.; Wu, X. L.; Guo, Y. G.; Zhong, Y. T.; Cao, X. Q.; Ma, Y.; Yao, J. N. Synthesis and Lithium Storage Properties of Co_3O_4 Nanosheet-Assembled Multishelled Hollow Spheres. *Adv. Funct. Mater.* **2010**, *20*, 1680–1686.
11. Venugopal, N.; Lee, D. J.; Lee, Y. J.; Sun, Y. K. Self-Assembled Hollow Mesoporous Co_3O_4 Hybrid Architectures: A Facile Synthesis and Application in Li-Ion Batteries. *J. Mater. Chem. A* **2013**, *1*, 13164–13170.
12. Lin, J.; Raji, A. R. O.; Nan, K. W.; Peng, Z. W.; Yan, Z.; Samuel, E. L. G.; Natelson, D.; Tour, J. M. Iron Oxide Nanoparticle and Graphene Nanoribbon Composite as an Anode Material for High-Performance Li-Ion Batteries. *Adv. Funct. Mater.* **2013**, *24*, 2044–2048.
13. Gao, G. X.; Yu, L.; Wu, H. B.; Lou, X. W. Hierarchical Tubular Structures Constructed by Carbon-Coated α-Fe_2O_3 Nanorods for Highly Reversible Lithium Storage. *Small* **2014**, *10*, 1741–1745.
14. Xu, M. W.; Wang, F.; Zhang, Y.; Yang, S.; Zhao, M. S.; Song, X. P. Co_3O_4-Carbon Nanotube Heterostructures with Bead-on-String Architecture for Enhanced Lithium Storage Performance. *Nanoscale* **2013**, *7*, 8067–8072.
15. Zhu, Q. L.; Li, J.; Xu, Q. Immobilizing Metal Nanoparticles to Metal–Organic Frameworks with Size and Location Control for Optimizing Catalytic Performance. *J. Am. Chem. Soc.* **2013**, *135*, 10210–10213.
16. Huang, Y. B.; Zhang, Y. H.; Chen, X. X.; Wu, D. S.; Yi, Z. G.; Cao, R. Bimetallic Alloy Nanocrystals Encapsulated in ZIF-8 for Synergistic Catalysis of Ethylene Oxidative Degradation. *Chem. Commun.* **2014**, *50*, 10115–10117.
17. Ju, P.; Jiang, L.; Lu, T. B. An Unprecedented Dynamic Porous Metal–Organic Framework Assembled from Fivefold Interlocked Closed Nanotubes with Selective Gas Adsorption Behaviors. *Chem. Commun.* **2013**, *49*, 1820–1822.
18. Teufel, J.; Oh, H.; Hirscher, M.; Wahiduzzaman, M.; Zhechkov, L.; Kuc, A.; Heine, T.; Denysenko, D.; Volkmer, D. MFU-4 – A Metal-Organic Framework for Highly Effective H_2/D_2 Separation. *Adv. Mater.* **2013**, *25*, 635–639.
19. Ke, F.; Yuan, Y. P.; Qiu, L. G.; Shen, Y. H.; Xie, A. J.; Zhu, J. F.; Tian, X. Y.; Zhang, L. D. Facile Fabrication of Magnetic Metal–Organic Framework Nanocomposites for Potential Targeted Drug Delivery. *J. Mater. Chem.* **2011**, *21*, 3843–3848.
20. Choi, K. M.; Jeong, H. M.; Park, J. H.; Zhang, Y. B.; Kang, J. K.; Yaghi, O. M. Supercapacitors of Nanocrystalline Metal–Organic Frameworks. *ACS Nano* **2014**, *8*, 7451–7457.

21. Hu, L.; Chen, Q. W. Hollow/Porous Nanostructures Derived from Nanoscale Metal–Organic Frameworks towards High Performance Anodes for Lithium-Ion Batteries. *Nanoscale* **2014**, *16*, 1236–1257.
22. Zhou, J. W.; Li, R.; Fan, X. X.; Chen, Y. F.; Han, R. D.; Li, W.; Zheng, J.; Wang, B.; Li, X. G. Rational Design of a Metal–Organic Framework Host for Sulfur Storage in Fast, Long-Cycle Li–S Batteries. *Energy Environ. Sci.* **2014**, *7*, 2715–2724.
23. Wu, R. B.; Qian, X. K.; Rui, X. H.; Liu, H.; Yadian, B. L.; Zhou, K.; Wei, J.; Yan, Q. Y.; Feng, X. Q.; Long, Y.; *et al*. Zeolitic Imidazolate Framework 67-Derived High Symmetric Porous Co_3O_4 Hollow Dodecahedra with Highly Enhanced Lithium Storage Capability. *Small* **2014**, *10*, 1932–1938.
24. Zou, F.; Hu, X. L.; Li, Z.; Qie, L.; Hu, C. C.; Zeng, R.; Jiang, Y.; Huang, Y. H. MOF-Derived Porous ZnO/$ZnFe_2O_4$/C Octahedra with Hollow Interiors for High-Rate Lithium-Ion Batteries. *Adv. Mater.* **2014**, *26*, 6622–6628.
25. Huang, G.; Zhang, L. L.; Zhang, F. F.; Wang, L. M. Metal–Organic Framework Derived Fe_2O_3@$NiCo_2O_4$ Porous Nanocages as Anode Materials for Li-Ion Batteries. *Nanoscale* **2014**, *6*, 5509–5515.
26. Huang, G.; Zhang, F. F.; Zhang, L. L.; Du, X. C.; Wang, J. W.; Wang, L. M. Hierarchical $NiFe_2O_4$/Fe_2O_3 Nanotubes Derived from Metal Organic Frameworks for Superior Lithium Ion Battery Anodes. *J. Mater. Chem. A* **2014**, *2*, 8048–8053.
27. Xu, X. D.; Cao, R. G.; Jeong, S.; Cho, J. Spindle-Like Mesoporous α-Fe_2O_3 Anode Material Prepared from MOF Template for High-Rate Lithium Batteries. *Nano Lett.* **2012**, *12*, 4988–4991.
28. Zhang, L.; Wu, H. B.; Madhavi, S.; Hng, H. G.; Lou, X. W. Formation of Fe_2O_3 Microboxes with Hierarchical Shell Structures from Metal–Organic Frameworks and Their Lithium Storage Properties. *J. Am. Chem. Soc.* **2012**, *134*, 17388–17391.
29. Wu, R. B.; Qian, X. K.; Zhou, K.; Wei, J.; Lou, J.; Ajayan, P. M. Porous Spinel $Zn_xCo_{3-x}O_4$ Hollow Polyhedra Templated for High-Rate Lithium-Ion Batteries. *ACS Nano* **2014**, *8*, 6297–6303.
30. Kim, S. W.; Ryu, J.; Park, C. B.; Kang, K. Carbon Nanotube-Amorphous $FePO_4$ Core-Shell Nanowires as Cathode Material for Li-Ion Batteries. *Chem. Commun.* **2010**, *46*, 7409–7411.
31. Fang, D.; Li, L. C.; Xu, W. L.; Li, G. Z.; Li, G.; Wang, N. F.; Luo, Z. P.; Xu, J.; Liu, L.; Huang, C. L.; *et al*. Self-Assembled Hairy Ball-Like Co_3O_4 Nanostructures for Lithium Ion Batteries. *J. Mater. Chem. A* **2013**, *1*, 13203–13208.
32. Xiao, Y.; Hu, C. W.; Cao, M. H. High Lithium Storage Capacity and Rate Capability Achieved by Mesoporous Co_3O_4 Hierarchical Nanobundles. *J. Power Sources* **2014**, *247*, 49–56.
33. Bai, Z. C.; Ju, Z. C.; Guo, C. L.; Qian, Y. T.; Tang, B.; Xiong, S. L. Direct Large-Scale Synthesis of 3D Hierarchical Mesoporous NiO Microspheres as High-Performance Anode Materials for Lithium Ion Batteries. *Nanoscale* **2014**, *6*, 3268–3273.
34. Huang, G.; Zhang, F. F.; Du, X. C.; Wang, J. W.; Yin, D. M.; Wang, L. M. Core–Shell $NiFe_2O_4$@TiO_2 Nanorods: an Anode Material with Enhanced Electrochemical Performance for Lithium-Ion Batteries. *Chem.—Eur. J.* **2014**, *35*, 11214–11219.
35. Shi, Y. F.; Guo, B. K.; Corr, S. A.; Shi, Q. H.; Hu, Y. S.; Heier, K. R.; Chen, L. Q.; Seshadri, R.; Stucky, G. D. Ordered Mesoporous Metallic MoO_2 Materials with Highly Reversible Lithium Storage Capacity. *Nano Lett.* **2009**, *9*, 4215–4220.